Frontiers in Bioscience Landmark

Front. Biosci. (Landmark Ed) **2026**; 31(8): 54109
https://doi.org/10.31083/FBL54109

Original Research

PDE4DIP-Derived MMG8 Supports Proliferation, Migration, and Tumor Growth in Hepatocellular Carcinoma Models

Cong Wang[1], Chunjing Bian[1], Tao Luo[1,2,*]

[1]Department of General Surgery, Xuanwu Hospital, Capital Medical University, 100053 Beijing, China
[2]National Clinical Research Center for Geriatric Diseases, 100053 Beijing, China
*Correspondence: taoluo35@126.com (Tao Luo)
Academic Editor: Jordi Sastre-Serra
Submitted: 21 May 2026 Revised: 29 June 2026 Accepted: 8 July 2026 Published: 14 August 2026

Abstract

Background: *PDE4DIP* encodes a scaffold protein that has been implicated in compartmentalized signaling and cytoskeletal organization, but the role of its myomegalin variant 8 (MMG8) isoform in hepatocellular carcinoma (HCC) remains unclear. To address this gap, we examined *PDE4DIP* expression in public HCC datasets and investigated the functional role of MMG8 in HCC models. **Methods:** *PDE4DIP* expression was analyzed in The Cancer Genome Atlas Liver Hepatocellular Carcinoma (TCGA-LIHC) cohort and two Gene Expression Omnibus (GEO) cohorts (GSE14520, GSE36376). MMG8 function was assessed in Huh7 cells using siRNA-mediated knockdown and in Hepa1-6 cells using lentiviral Clustered Regularly Interspaced Short Palindromic Repeats - CRISPR-associated protein 9 (CRISPR-Cas9)-mediated knockout. Cell proliferation in MMG8-KD Huh7 cells and MMG8-KO Hepa1-6 cells was assessed using Cell Counting Kit-8 (CCK-8) assays, while Huh7 cell migration was evaluated using Transwell assays. Tumor growth was assessed using a murine subcutaneous tumor model. Immunohistochemical staining for Ki67 and cleaved caspase-3 was employed to assess tumor cell proliferation and apoptosis-associated changes, respectively. Gene set enrichment analysis was performed in TCGA-LIHC tumors stratified based on *PDE4DIP* expression. **Results:** *PDE4DIP* expression differed between tumor and non-tumor tissues across HCC cohorts, although the directionality of this difference was not uniform. MMG8 knockdown in Huh7 cells reduced proliferation and migratory activity. A single-cell-derived MMG8-KO Hepa1-6 clone exhibited reduced proliferation *in vitro* and formed smaller tumors *in vivo*, with lower Ki67 positivity but no significant difference in cleaved caspase-3 positivity between groups. In tumors from the TCGA-LIHC cohort, *PDE4DIP* expression was associated with distinct transcriptional programs. Specifically, *PDE4DIP*-high tumors presented with positive normalized enrichment score (NES) values for several metabolic pathways, whereas adhesion/extracellular matrix (ECM), cell cycle/proliferation, and translation/ribosome-related pathways exhibited negative NES values. **Conclusions:** These findings support a functional contribution of MMG8 to proliferative, migratory, and tumor-growth phenotypes in the tested HCC models. Bulk gene-level *PDE4DIP* expression in human tumors was associated with context-dependent transcriptional states and should not be interpreted as a direct surrogate for MMG8 function.

Keywords: *PDE4DIP*; MMG8; hepatocellular carcinoma; proliferation; migration; tumor growth

1. Introduction

Hepatocellular carcinoma (HCC) develops through convergent pressures imposed by chronic liver injury, viral infection, metabolic dysfunction, fibrosis, and inflammatory remodeling. Rather than giving rise to a uniform disease, these etiological factors contribute to the emergence of heterogeneous HCC tumors that fall into transcriptional and genetic subgroups with different proliferative, metabolic, immune, and stromal features, constraining efforts to interpret data for any given bulk expression marker [1,2,3,4]. This heterogeneity is particularly relevant when evaluating genes that encode products that exert their effects through changes in spatial organization rather than direct enzymatic activity.

PDE4DIP encodes myomegalin, a large Golgi and centrosome-associated scaffold protein. Myomegalin was originally identified as a phosphodiesterase 4D (PDE4D)-interacting protein with a muscle-enriched expression pattern linked to compartmentalized cyclic adenosine monophosphate (cAMP) signaling [5]. Subsequent work revealed that myomegalin contributes to centrosomal and Golgi-derived microtubule organization [6]. A distinct isoform of this protein, myomegalin variant 8 (MMG8), localizes predominantly to *cis*-Golgi networks through interaction with A-Kinase Anchoring Protein 450/A-Kinase Anchoring Protein 9 (AKAP450/AKAP9) and participates in Golgi microtubule organization and endoplasmic reticulum (ER)-Golgi transport [7]. These observations suggest that MMG8 functions at the interface of compartmentalized signaling, microtubule architecture, and intracellular trafficking.

In addition to dependence on the transcriptional activation of growth-associated genes, the proliferation and migration of cancer cells depend on the spatial orientations of specific signaling molecules, cytoskeletal regulators, and components of the membrane trafficking ma-

chinery. A-kinase anchoring proteins and related scaffolds can coordinate signaling output by restricting kinases, phosphatases, and phosphodiesterases to defined subcellular compartments [8,9]. Given these complex localization-based dynamics, simply examining gene expression may fail to adequately predict gene function, as isoform usage, subcellular localization, and protein complex composition can determine whether a scaffold ultimately supports growth, motility, or tissue-level expansion.

Studies on *PDE4DIP* in the context of HCC remain lacking. Public transcriptomic datasets can offer insight into whether *PDE4DIP* expression differs across liver cancer cohorts, but they cannot establish whether MMG8 itself controls malignant cell behavior. This distinction is important, as bulk RNA-seq integrates signals from tumor cells, stromal cells, immune infiltrates, and vascular components, with their relative contributions varying according to tumor purity. It is thus important to differentiate between gene-level associations for *PDE4DIP* in HCC and outcomes associated with the direct perturbation of MMG8 in experimental models.

To address this gap, we combined public cohort analyses and loss-of-function experiments to probe both *PDE4DIP* at the gene level and MMG8 functionality in HCC. We first assessed *PDE4DIP* expression in The Cancer Genome Atlas Liver Hepatocellular Carcinoma (TCGA-LIHC) and independent Gene Expression Omnibus (GEO) HCC cohorts. We then tested MMG8 function in HCC cell models using knockdown or knockout strategies, followed by proliferation and migration assays, assessment of subcutaneous tumor growth, and immunohistochemical (IHC) staining for Ki67 and cleaved caspase-3. Finally, we examined *PDE4DIP*-associated pathways in TCGA-LIHC tumor samples using a gene set enrichment analysis approach. This design allowed us to distinguish between two related questions: whether gene-level *PDE4DIP* expression is associated with altered transcriptional states in human HCC, and whether MMG8 contributes functionally to tumor cell growth and migration in the models tested.

2. Materials and Methods

2.1 Public HCC Transcriptomic Datasets

Transcriptomic and clinical data for the TCGA-LIHC cohort were obtained from the National Cancer Institute (NCI) Genomic Data Commons (GDC) portal [10]. RNA-seq expression data were processed as harmonized gene-level expression matrices. *PDE4DIP* expression was extracted from the corresponding gene annotation and expressed as log2(TPM + 1) values from the harmonized tpm_unstrand field. Normal liver and primary tumor samples were identified using TCGA sample barcodes, with samples bearing code "11" classified as normal tissues and those bearing code "01" classified as primary tumor tissues. The overall tumor-versus-normal comparison was performed using the Wilcoxon rank-sum test, and matched tumor-normal pairs were identified based on patient barcodes and analyzed using the paired Wilcoxon signed-rank test.

The GSE14520 and GSE36376 datasets were accessed through the GEO database [11]. Processed expression matrices were used to analyze these GEO datasets. Probe-set expression summaries were interpreted according to the corresponding platform annotations. For the sample-level expression values shown in Fig. 1B,C, the arithmetic mean of the expression values from five selected platform-specific *PDE4DIP* probes was calculated within each sample before between-group comparison using the Wilcoxon rank-sum test. Probe-level consistency was examined separately within each dataset and platform, and no cross-platform probe collapsing or merging was performed. Platform-level *PDE4DIP* probe annotations were re-examined, and probe-level tumor-versus-adjacent/non-tumor differences were assessed using the Wilcoxon rank-sum test with Benjamini-Hochberg adjustment. Because the cohorts were generated using different microarray platforms and exact cross-platform exon equivalence could not be established, all GEO findings were interpreted as gene-level *PDE4DIP* evidence rather than MMG8 isoform-specific or exon-specific expression evidence (**Supplementary Table 1**).

2.2 Cell Culture

The human Huh7 HCC cell line (Cat. No. CL-0120) and the murine Hepa1-6 hepatoma cell line (Cat. No. CL-0105) were obtained from Wuhan Pricella Biotechnology Co., Ltd. (Wuhan, Hubei, China). All cell lines were authenticated by short tandem repeat (STR) profiling, routinely tested, and confirmed to be free of mycoplasma contamination. Cells were cultured in Dulbecco's modified Eagle's medium (DMEM; Cat. No. C11995500BT; Gibco, Grand Island, NY, USA) containing 10% fetal bovine serum (FBS; Cat. No. A5256701; Gibco) and 1% penicillin-streptomycin (Cat. No. 15140-122; Gibco). Cells were maintained at 37 °C in a humidified incubator with 5% CO_2.

2.3 SiRNA-Mediated MMG8 Knockdown in Huh7 Cells

To investigate the function of MMG8 in Huh7 cells, these cells were transfected with one previously reported MMG8-targeting siRNA duplex (si-MMG8-1 [7]) or a universal non-targeting control siRNA at a final concentration of 50 nM using Lipofectamine 3000 (Cat. No. L3000015; Invitrogen, Carlsbad, CA, USA) according to the manufacturer's instructions. All siRNAs were obtained from GenePharma (Shanghai, China); MMG8 siRNA: 5′-AACCUCCAGUGGCUGAAAGAA-3′ (sense) and 5′-UUCUUUCAGCCACUGGAGGUU-3′ (antisense); negative control siRNA: 5′-UUCUCCGAACGUGUCACGUTT-3′ (sense) and 5′-ACGUGACACGUUCGGAGAATT-3′ (antisense).

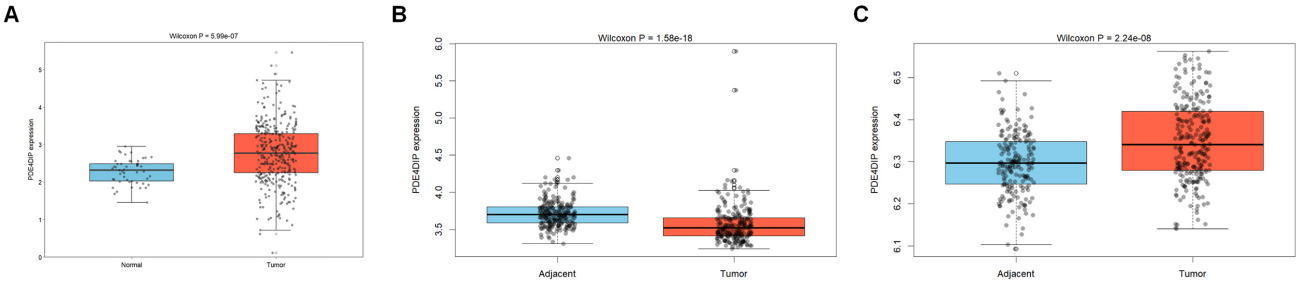

Fig. 1. *PDE4DIP* expression exhibits cohort-dependent differences when comparing HCC and non-tumor tissues. (A) Gene-level *PDE4DIP* expression in solid tissue normal liver samples and primary solid tumors from the TCGA-LIHC cohort, analyzed using log2(TPM + 1) values derived from tpm_unstrand (371 tumors and 50 solid tissue normal samples). (B) *PDE4DIP* expression in adjacent non-tumor tissues and tumor tissues from the GSE14520 cohort. (C) *PDE4DIP* expression in adjacent non-tumor tissues and tumor tissues from the GSE36376 cohort. Data are shown as box plots, with individual samples overlaid. *p*-values were calculated using Wilcoxon rank-sum tests. GEO measurements represent gene-level *PDE4DIP* signals; cross-platform exon equivalence and MMG8 isoform specificity could not be established (**Supplementary Table 1**). HCC, hepatocellular carcinoma; TCGA-LIHC, The Cancer Genome Atlas Liver Hepatocellular Carcinoma; GEO, Gene Expression Omnibus; MMG8, myomegalin variant 8.

Cells transfected with the MMG8-targeting siRNA were designated as MMG8-KD cells, while cells transfected with negative control siRNA were designated as control cells. Knockdown efficiency was evaluated by Western blotting. At 48 h post-transfection, cells were either harvested for Western blotting or reseeded at equal densities for the Cell Counting Kit-8 (CCK-8) and Transwell assays. Transient siRNA-mediated knockdown was used because the Huh7 experiments were designed as short-term *in vitro* assays to evaluate the effects of MMG8 knockdown.

2.4 Generation of MMG8 Knockout Hepa1-6 Cells

MMG8 knockout Hepa1-6 cells were generated using a lentiviral Clustered Regularly Interspaced Short Palindromic Repeats/CRISPR-associated protein 9 (CRISPR-Cas9) system. The lentiCRISPRv2 vector was kindly provided by Prof. Zhe Wang (Xuanwu Hospital, Capital Medical University, Beijing, China). A single sgRNA targeting murine *Pde4dip* was cloned into the lentiCRISPRv2 vector. The 20-nt protospacer sequence was 5′-AGCCCATTCAGAGTCCCAGA-3′ and was followed by a GGG protospacer-adjacent motif (PAM). Correct insertion of the sgRNA sequence into lentiCRISPRv2 was confirmed by Sanger sequencing. Control cells were generated using the empty lentiCRISPRv2 vector.

Hepa1-6 cells were transduced with the sequence-verified lentiviral CRISPR-Cas9 construct or empty vector control, followed by selection with puromycin at 3 μg/mL (Cat. No. A1113802; Gibco). Surviving cells were expanded, and single-cell-derived colonies were manually picked under a microscope from both populations. Individual clones were screened by Western blotting for loss of the detectable 443M-reactive band at the expected molecular weight corresponding to MMG8, and one single-cell-derived empty-vector control clone and one single-cell-derived MMG8-KO clone were used for subsequent experiments. A stable CRISPR-Cas9 knockout clone was used for *in vivo* experiments owing to the need for the sustained loss of MMG8 during cell expansion, subcutaneous inoculation, and longitudinal tumor growth.

2.5 Western Blotting

Western blotting was used to validate MMG8 knockdown in Huh7 cells and confirm loss of the detectable 443M-reactive band at the expected molecular weight corresponding to MMG8 in the selected Hepa1-6 clone. Total protein was extracted using radioimmunoprecipitation assay (RIPA) lysis buffer (Cat. No. G2002-100ML; Servicebio, Wuhan, Hubei, China) supplemented with a protease inhibitor cocktail (Cat. No. G2006-250UL; Servicebio). Protein concentrations were determined using a Bicinchoninic acid (BCA) Protein Assay Kit (Cat. No. PC0020; Solarbio, Beijing, China). Equal amounts of protein were separated by sodium dodecyl sulfate polyacrylamide gel electrophoresis (SDS-PAGE) and transferred onto polyvinylidene fluoride (PVDF) membranes (Cat. No. IPVH00010; Millipore, Billerica, MA, USA). After blocking, membranes were incubated with the rabbit polyclonal 443M antibody raised against amino acids 637–925 of human MMG8 (1:1000; in-house generated and previously characterized [7]) and rabbit anti-β-actin (1:5000; Cat. No. 4967S; Cell Signaling Technology, Danvers, MA, USA), followed by an HRP-conjugated goat anti-rabbit IgG (H+L) secondary antibody (1:2000; Cat. No. SA00001-2; Proteintech, Wuhan, Hubei, China).

Immunoreactive bands were developed using Immobilon Western Chemiluminescent HRP Substrate (Cat. No. WBKLS0100; Millipore) and visualized using a Tanon-5200 chemiluminescence imaging system (Tanon Science & Technology Co., Ltd., Shanghai, China). β-actin was used as the loading control. For densitometric analyses, band intensity was quantified using ImageJ v1.54p (Na-

tional Institutes of Health, Bethesda, MD, USA). The intensity of the 443M-reactive band at the expected molecular weight corresponding to MMG8 was normalized to β-actin for each lane, and normalized values were expressed relative to the control group.

2.6 CCK-8 Cell Proliferation Assay

Cell proliferation was assessed using the CCK-8 (Cat. No. CA1210; Solarbio, Beijing, China). Control and MMG8-KD Huh7 cells, as well as the single-cell-derived empty-vector control clone and the single-cell-derived MMG8-KO Hepa1-6 clone, were seeded into 96-well plates at 2000 cells per well. At 0, 24, 48, and 72 h, CCK-8 reagent was added according to the manufacturer's protocol, and absorbance at 450 nm was measured using an Infinite F50 microplate reader (Tecan Group Ltd., Männedorf, Switzerland). Cell-free wells containing culture medium and CCK-8 reagent were used for background correction. Measurements were obtained in three independent experiments, each including three technical replicate wells per group at each time point, with all technical replicates being averaged before statistical analysis. Huh7 assay results were graphed by expressing background-corrected values relative to the corresponding value at the 0 h time point.

2.7 Transwell Migration Assay

Cell migration was assessed using Transwell chambers with an 8-μm pore size (Cat. No. 3422; Corning Inc., Corning, NY, USA). Control and MMG8-KD Huh7 cells were suspended in serum-free medium and seeded into the upper chamber at 60,000 cells per insert. The lower chamber was filled with medium supplemented with 10% FBS. After incubating these cells for 24 h, non-migrated cells on the upper surface of the membrane were removed, whereas those that had migrated to the lower surface were fixed with 4% paraformaldehyde (Cat. No. P1110; Solarbio, Beijing, China) and stained with crystal violet (Cat. No. C8470; Solarbio, Beijing, China).

Images were acquired using a BZ-X810 microscope (Keyence Corporation, Osaka, Japan) with a 10× objective. For each biological replicate, migrated cells in multiple microscopic fields were counted and averaged together to establish a replicate-level value. Three biological replicates per group were used for subsequent statistical analysis.

2.8 Mouse Subcutaneous Tumor Model

All animal experimental protocols were approved by the Animal Ethics Committee of the Laboratory Animal Center, Xuanwu Hospital, Capital Medical University, China (XW-20210420-10). Female C57BL/6 mice (5 week-old) were purchased from Vital River Laboratory Animal Technology Co., Ltd. (Beijing, China). Mice were housed under specific pathogen-free conditions with controlled temperature, humidity, and light-dark cycle. Female mice were used in accordance with the established subcutaneous tumor protocol in our laboratory and to facilitate stable group housing while minimizing aggression-related injury and stress.

Control and MMG8-KO Hepa1-6 cells were harvested during the logarithmic phase of growth, washed, and resuspended in a 1:1 mixture of PBS and Matrigel (Cat. No. 356234; Corning Inc.). A total of 2×10^6 cells were injected subcutaneously into the right upper abdominal region of each mouse after randomizing mice into the control and MMG8-KO groups (n = 5/group).

Tumor dimensions were measured using a 16 ES digital caliper (Mahr GmbH, Göttingen, Germany) at the indicated time points, and tumor volume was calculated as length × width^2 / 2. Tumor dimensions were measured by an investigator who remained blinded to group allocation. No animals or measurements of tumor volume were excluded from the analysis. At the experimental endpoint, mice were anesthetized by intraperitoneal injection of sodium pentobarbital (Sinopharm Chemical Reagent Co., Ltd., Shanghai, China; batch No. WS20050411) at 100 mg/kg. After adequate anesthesia was confirmed, mice were euthanized by cervical dislocation. Tumors were then excised, photographed, and processed for histological analysis.

2.9 Immunohistochemistry and Image Quantification

Ki67 and cleaved caspase-3 immunohistochemistry (IHC) staining and image quantification were performed by Wuhan Servicebio Technology Co., Ltd. (Wuhan, Hubei, China). Paraffin-embedded tumor sections were subjected to marker-specific antigen retrieval. For Ki67 staining, citrate buffer (pH 6.0; Cat. No. G1202; Servicebio) was used under high pressure for 3 min; for cleaved caspase-3 staining, Tris-EDTA buffer (pH 8.0; Cat. No. G1206; Servicebio) was used at 100 °C for 15 min. After antigen retrieval, sections were blocked with 3% bovine serum albumin (BSA) for 30 min and incubated at 4 °C overnight with an anti-Ki67 antibody (1:500; Cat. No. GB111499; Servicebio) or an anti-cleaved caspase-3 rabbit polyclonal antibody (1:500; Cat. No. GB11532; Servicebio), respectively.

Sections were then incubated for 50 min at room temperature with a ready-to-use S-vision polymer goat anti-rabbit secondary antibody (Cat. No. G1302; Servicebio), developed with 3,3′-Diaminobenzidine (DAB) (Cat. No. G1212; Servicebio), and counterstained with hematoxylin. Stained sections were digitized using an LG-S80 slide scanner (Servicebio).

Ki67 positivity was quantified as the percentage of Ki67-positive nuclei among total nuclei, whereas cleaved caspase-3 positivity was quantified as the percentage of positive cells among total cells. For each marker, 15 non-overlapping 300 × 300-pixel rectangular regions were analyzed per tumor at 20× magnification, and the 15 region-

level values were averaged to generate one tumor-level value for statistical analysis. Five tumor samples per group were analyzed. Personnel performing image quantification for both markers were blinded to group identity, and no tumor samples were excluded.

2.10 Gene Set Enrichment Analysis

To examine transcriptional programs associated with *PDE4DIP* expression in HCC tumors, TCGA-LIHC primary tumor samples were stratified into *PDE4DIP*-high and *PDE4DIP*-low groups using the median *PDE4DIP* expression value. Differential expression analysis between the two groups was performed using raw gene-level count data in DESeq2 v1.50.2 (https://bioconductor.org/packages/3.22/bioc/html/DESeq2.html), and genes were ranked according to the Wald statistic for gene set enrichment analysis (GSEA).

GSEA was performed using a preranked GSEA approach [12] implemented with the R package fgsea v1.36.2. Hallmark, Kyoto Encyclopedia of Genes and Genomes (KEGG) Legacy, KEGG Medicus, and Reactome gene sets were obtained from release 2026.1. Hs of the Molecular Signatures Database (MSigDB) [13]. Hallmark gene sets were obtained from collection H, whereas KEGG Legacy, KEGG Medicus, and Reactome pathways were obtained from the C2 curated collection using the CP: KEGG_LEGACY, CP: KEGG_MEDICUS, and CP: REACTOME subcollections, respectively. Pathways were ranked based on normalized enrichment score (NES) values, with positive and negative NES values indicating enrichment in the *PDE4DIP*-high and *PDE4DIP*-low groups, respectively. False discovery rate (FDR) correction was used to account for multiple testing. Corresponding gene-set files were generated using msigdbr version 26.1.0 (https://igordot.github.io/msigdbr/).

2.11 Statistical Analysis

In vitro experimental data were analyzed and visualized using GraphPad Prism 10.1.2 (GraphPad Software, Boston, MA, USA). Bioinformatic and public-cohort analyses were performed in R v4.5.3 (R Foundation for Statistical Computing, Vienna, Austria). Data are presented as mean ± SD unless otherwise stated.

For comparisons between two groups, two-tailed unpaired Student's *t*-tests or Welch's *t*-tests were used as appropriate. Wilcoxon rank-sum and paired Wilcoxon signed-rank tests were used for unpaired and matched comparisons of public transcriptomic datasets, respectively. For the Huh7 CCK-8 assay, group comparisons were performed at each time point. Hepa1-6 CCK-8 data were analyzed by two-way repeated-measures Analysis of Variance (ANOVA) with independent experiment as the matched subject; Geisser–Greenhouse correction was applied, followed by Šídák-adjusted between-group comparisons at individual time points. Transwell migration data and Ki67 and cleaved caspase-3 positivity were each analyzed using Welch's *t*-test. Longitudinal tumor-volume data were analyzed by two-way repeated-measures ANOVA with mouse as the repeated-measures subject and Greenhouse–Geisser correction; Holm-adjusted between-group comparisons were performed at individual time points. Tumor growth burden was also assessed by individual-mouse area under the curve (AUC) analysis, with AUC values compared using Welch's *t*-test. The repeated-measures analysis was repeated after log transformation as a sensitivity analysis. A two-sided p value < 0.05 was considered statistically significant.

For TCGA-LIHC clinicopathological, tumor-purity, and survival analyses, the same log2(TPM + 1) values derived from tpm_unstrand were used. Associations with AJCC pathological stage, tumor grade, and Ishak fibrosis group were evaluated using Kruskal–Wallis tests. Participant barcodes were used to match ABSOLUTE purity estimates from the TCGA Pan-Cancer Atlas [14,15], which were assessed using Spearman and Pearson correlations. Overall survival in 366 primary tumors was analyzed using the survival package v3.8-6 by median-split Kaplan–Meier/log-rank analysis and continuous univariate and multivariable Cox regression adjusted for age, gender, stage, and grade; fibrosis- and purity-adjusted models were examined as sensitivity analyses, and proportional-hazards assumptions were assessed. Recurrence-free survival was not modeled because recurrence-time data were unavailable. Detailed specifications are provided in **Supplementary Table 2**.

3. Results

3.1 PDE4DIP Expression Differs Across HCC Cohorts

We began by examining *PDE4DIP* expression in public HCC datasets. In the TCGA-LIHC cohort, gene-level *PDE4DIP* expression was higher in primary solid tumors than in solid tissue normal liver samples based on log2(TPM + 1) values derived from tpm_unstrand (371 tumors vs. 50 solid tissue normal samples; Wilcoxon $p = 5.992 \times 10^{-7}$; Fig. 1A). A consistent increase was also observed in 50 matched tumor-normal pairs (paired Wilcoxon $p = 9.246 \times 10^{-5}$; **Supplementary Table 2**). This pattern was reproduced in the GSE36376 cohort, where tumor samples exhibited higher levels of *PDE4DIP* expression relative to adjacent non-tumor tissues (Wilcoxon $p = 2.24 \times 10^{-8}$; Fig. 1C). In the GSE14520 cohort, however, lower *PDE4DIP* expression was noted in tumor tissues relative to adjacent tissues (Wilcoxon $p = 1.58 \times 10^{-18}$; Fig. 1B). Probe-level re-annotation supported these cohort-specific directions without establishing that the probes interrogated identical *PDE4DIP* exons across platforms or providing MMG8 isoform-specific resolution (**Supplementary Table 1**). These data thus suggest that *PDE4DIP* expression is transcriptionally altered in HCC cohorts, but the directionality of this alteration is not uniform across datasets.

This inconsistency argues against treating total *PDE4DIP* expression as a simple marker capable of differentiating tumors from normal tissue. Instead, the cohort-dependent pattern suggests that *PDE4DIP*-associated biology may depend on sample composition, platform, tumor context, or transcript-level differences not accessible when solely focusing on gene-level expression. Because gene-level *PDE4DIP* measurements are incapable of differentiating between MMG8 and other *PDE4DIP*-derived transcripts or tissue-derived signals, we focused subsequent functional experiments on MMG8, as this was the *PDE4DIP*-derived protein product selected for perturbation in our HCC model systems.

Additional TPM-based TCGA-LIHC analyses revealed no significant association between *PDE4DIP* expression and American Joint Committee on Cancer (AJCC) pathological stage, tumor grade, or Ishak fibrosis group (all $p \geq 0.305$). *PDE4DIP* expression was weakly correlated with ABSOLUTE tumor purity (Spearman $\rho = 0.211$, $p = 6.536 \times 10^{-5}$; Pearson $r = 0.203$, $p = 1.240 \times 10^{-4}$). Overall survival did not differ significantly between the median-defined *PDE4DIP*-high and *PDE4DIP*-low groups (log-rank $p = 0.123$; **Supplementary Fig. 1**). *PDE4DIP* expression was not significantly associated with overall survival in continuous univariate or multivariable Cox models; in the main adjusted model, the HR per one-unit increase in log2(TPM + 1) was 1.046 (95% CI = 0.843–1.298, $p = 0.684$). Fibrosis- and purity-adjusted sensitivity analyses yielded consistent results. Recurrence-free survival was not assessed because no valid recurrence-time values were available in the clinical annotation used to conduct these analyses (**Supplementary Table 2**).

3.2 MMG8 Knockdown Reduces Huh7 Cell Proliferation and Migration In Vitro

To test the potential contribution of MMG8 to malignant cellular behavior in HCC, we generated MMG8-knockdown Huh7 cells. Western blotting revealed a reduction in the intensity of the 443M-reactive band at the expected molecular weight corresponding to MMG8 in MMG8-KD cells compared with control cells, and densitometric analysis normalized to β-actin confirmed a consistent decrease in band intensity (Fig. 2A), validating this cellular model used for downstream functional assays.

Cell proliferation was next assessed via CCK-8 assay. Control Huh7 cells exhibited a progressive increase in relative proliferation over time, whereas MMG8-KD cells showed a slower increase in relative CCK-8 signal across the measured time course (Fig. 2B). At later time points, the separation between the two curves became increasingly evident, consistent with a reduction in proliferative activity following MMG8 knockdown.

We next examined cell migration using a Transwell assay. Fewer migrated cells were evident in representative images from the MMG8-KD group as compared to the control group (Fig. 2C). Biological replicate quantification based on multiple microscopic fields confirmed a reduction in migrated cells per field after MMG8 knockdown (two-tailed unpaired Welch's *t*-test, $p = 0.0019$; Fig. 2C). Together, these findings indicate that MMG8 knockdown reduces proliferative activity and migration in Huh7 cells.

3.3 MMG8 Knockout Reduces Hepa1-6 Cell Proliferation In Vitro

Prior to subcutaneous injection, we characterized and assessed the proliferative capacity of the single-cell-derived MMG8-KO Hepa1-6 clone relative to the single-cell-derived empty-vector control clone. Western blotting confirmed the loss of the detectable 443M-reactive band at the expected molecular weight corresponding to MMG8 in the MMG8-KO clone (Fig. 3A). Both groups exhibited comparable background-corrected OD450 values at 0 h, while the MMG8-KO cells exhibited a slower OD450 increase over the subsequent 72 h (Fig. 3B).

Two-way repeated-measures ANOVA with Geisser–Greenhouse correction revealed a significant group-by-time interaction ($F(1.833, 3.665) = 802.3$, $p < 0.0001$). Šídák-adjusted comparisons showed no significant difference at 0 h ($p = 0.9962$) or 24 h ($p = 0.0722$), whereas OD450 values were significantly lower in the MMG8-KO group at 48 h ($p = 0.0217$) and 72 h ($p = 0.0013$). These findings indicate that the MMG8-KO Hepa1-6 clone exhibited reduced proliferative capacity before subcutaneous injection.

3.4 An MMG8-KO Hepa1-6 Clone Exhibits Reduced Tumor Growth In Vivo

Based on the successful validation shown above, the control and MMG8-KO Hepa1-6 clones were next implanted in mice to characterize subcutaneous tumor growth. Tumor volume was measured longitudinally after cell inoculation. Tumors derived from control Hepa1-6 cells increased progressively over the observation period, whereas tumors derived from MMG8-KO cells remained smaller at each measured time point (Fig. 4A). Two-way repeated-measures ANOVA showed a significant group-by-time interaction after Greenhouse–Geisser correction ($F(1.24, 9.93) = 15.40$, $p = 0.0020$), indicating different tumor-growth trajectories between the groups. Individual-mouse AUC analysis further revealed lower cumulative tumor volume in the MMG8-KO group as compared to the control group (846.9 ± 110.3 vs. 1828.5 ± 342.6 $mm^3 \cdot day$; Welch's *t*-test, $p = 0.0020$). Secondary Holm-adjusted time-point comparisons and analysis of log-transformed tumor volumes did not alter the interpretation of the primary longitudinal analysis. These data indicated that tumors derived from the MMG8-KO Hepa1-6 clone grew more slowly *in vivo*.

Gross tumor images at the endpoint were consistent with the longitudinal measurements, such that tumors in the MMG8-KO group were smaller than those in the control

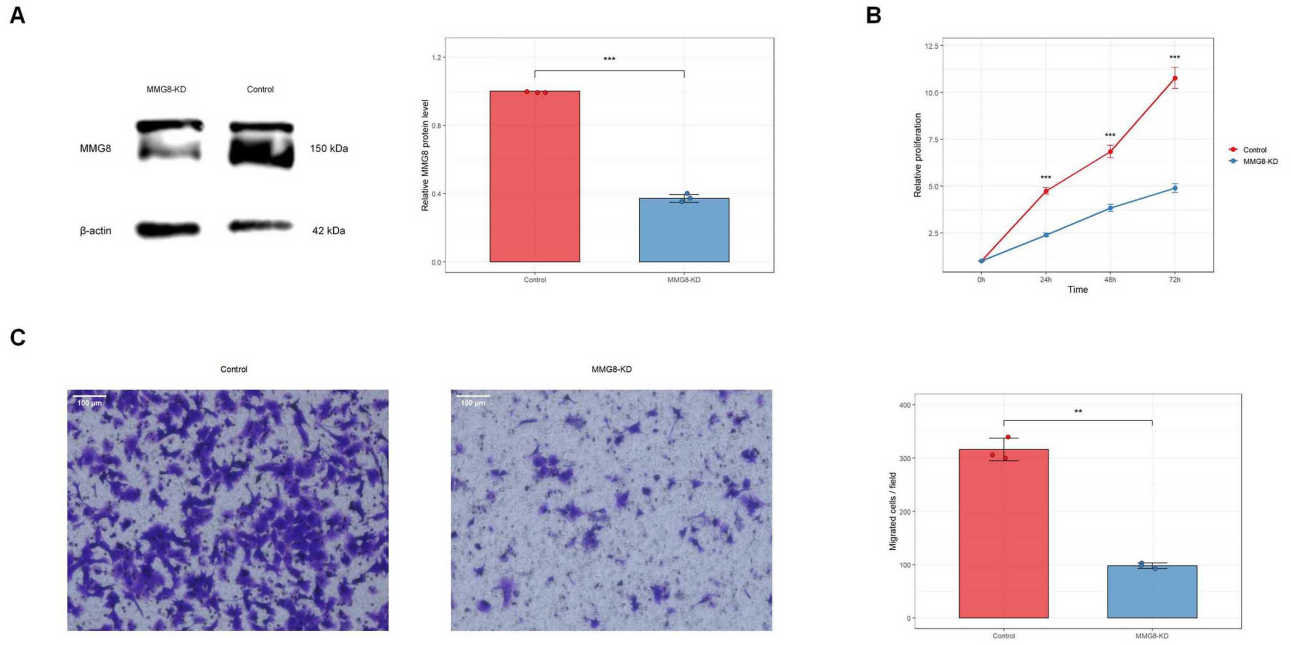

Fig. 2. MMG8 knockdown suppresses Huh7 cell proliferation and migration *in vitro*. (A) Representative Western blotting images of the 443M-reactive band at the expected molecular weight corresponding to MMG8 with densitometric quantification in control and MMG8-KD Huh7 cells. β-actin was used as the loading control, and normalized band intensity was expressed relative to the control. (B) Cell Counting Kit-8 (CCK-8) proliferation assay at 0, 24, 48, and 72 h. Background-corrected values were normalized to the corresponding 0-h value. Three technical replicates per group and time point were averaged within each of three independent experiments. (C) Representative Transwell images and corresponding quantification of Huh7 cell migration. Counts from multiple microscopic fields were averaged to generate one value per biological replicate (n = 3 per group). Images were acquired using a 10× objective. Scale bars, 100 μm. Data are presented as mean ± SD. Group comparisons were performed using two-tailed unpaired Student's or Welch's *t*-tests, as appropriate; Transwell data were compared using Welch's *t*-tests. $^{**}p < 0.01$, $^{***}p < 0.001$.

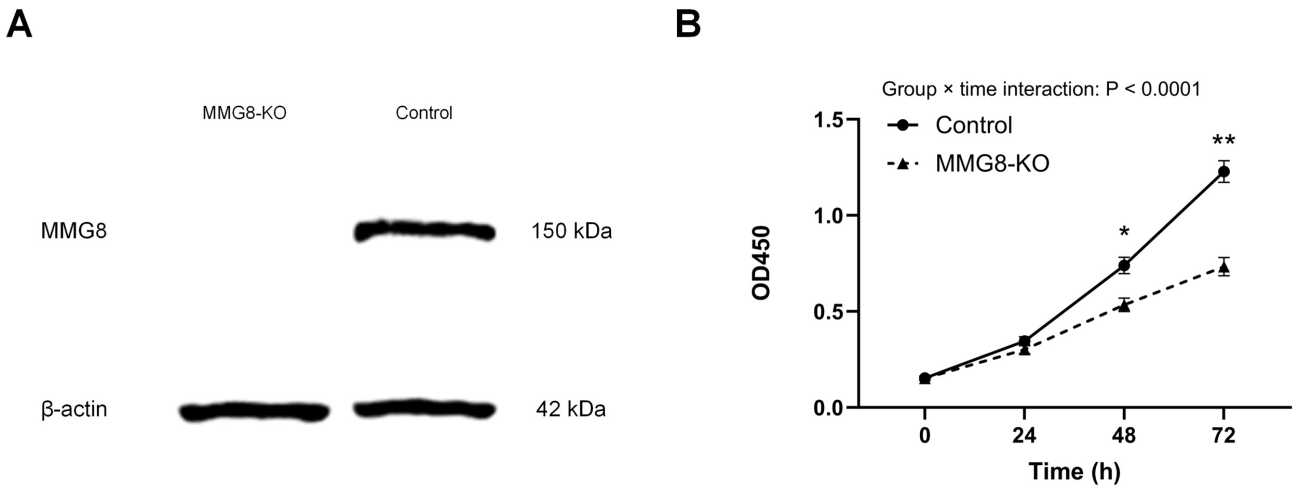

Fig. 3. MMG8 knockout reduces Hepa1-6 cell proliferation *in vitro*. (A) Representative Western blotting images showing loss of the detectable 443M-reactive band at the expected molecular weight corresponding to MMG8 in the single-cell-derived MMG8-KO Hepa1-6 clone compared with the single-cell-derived empty-vector control clone. β-actin was used as the loading control. (B) CCK-8 proliferation curves corresponding to the control and MMG8-KO Hepa1-6 cells based on background-corrected OD450 values at 0, 24, 48, and 72 h. Three technical wells per group and time point were averaged within each of three independent experiments. Data are presented as mean ± SD. Statistical significance was assessed using two-way repeated-measures Analysis of Variance (ANOVA) with Geisser–Greenhouse correction, followed by Šídák-adjusted comparisons between groups at individual time points. $^{*}p < 0.05$, $^{**}p < 0.01$.

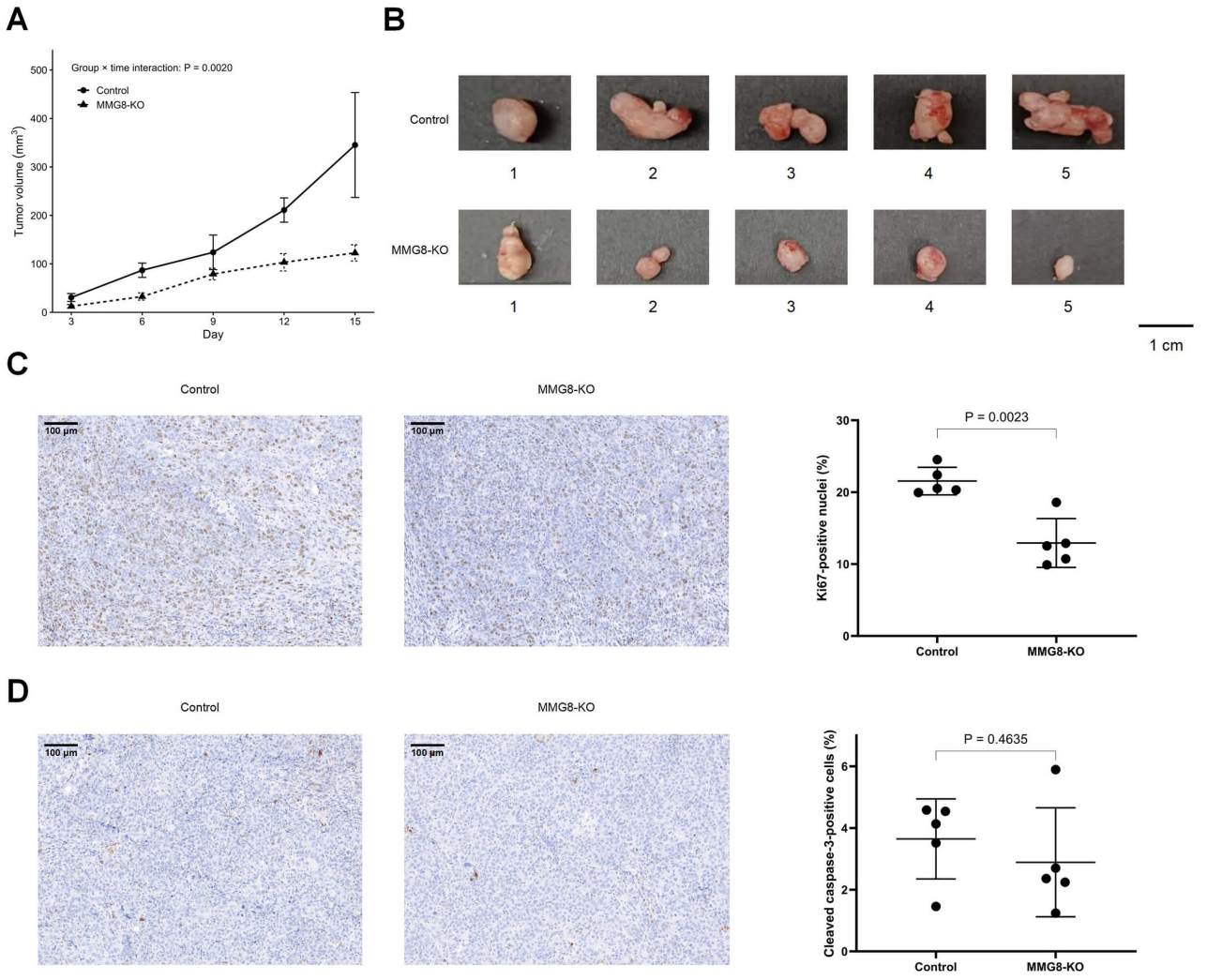

Fig. 4. An MMG8-KO Hepa1-6 clone shows reduced tumor growth and Ki67 positivity *in vivo*. (A) Tumor growth curves from mice subcutaneously implanted with control or MMG8-KO Hepa1-6 cells. (B) Images of all excised tumors from the control and MMG8-KO groups at the experimental endpoint. Scale bar, 1 cm. (C) Representative Ki67 immunohistochemistry images and corresponding quantification of Ki67-positive nuclei in tumor tissues from the control and MMG8-KO groups. Scale bars, 100 µm. (D) Representative cleaved caspase-3 immunohistochemistry images and corresponding quantification of cleaved caspase-3-positive cells in tumor tissues from the control and MMG8-KO groups. Scale bars, 100 µm. Data are presented as mean ± SD. Tumor growth was analyzed by two-way repeated-measures ANOVA with Greenhouse–Geisser correction; Ki67 and cleaved caspase-3 positivity were compared using two-tailed unpaired Welch's *t*-tests. For each marker, 15 non-overlapping 300 × 300-pixel regions were analyzed per tumor at 20× magnification and averaged to generate one tumor-level value; each point represents one tumor (n = 5 per group).

group (Fig. 4B). We next employed Ki67 IHC staining to assess tumor cell proliferation. Control tumors contained a higher fraction of Ki67-positive nuclei than MMG8-KO tumors, and corresponding quantification confirmed a reduction in Ki67 positivity after MMG8 knockout (two-tailed unpaired Welch's *t*-test, $p = 0.0023$; Fig. 4C). These Ki67 data provide a tissue-level correlate for the reduced tumor growth curve, and are consistent with diminished proliferative activity within the tumor tissue. To determine whether reduced tumor growth was accompanied by altered apoptotic activity, we performed immunohistochemical staining for cleaved caspase-3. Cleaved caspase-3 positivity did not differ significantly between control and MMG8-KO tumors (3.646 ± 1.297% vs. 2.888 ± 1.767%; two-tailed unpaired Welch's *t*-test, $p = 0.4635$; Fig. 4D). Thus, reduced tumor growth was accompanied by lower Ki67 positivity but without a statistically significant change in cleaved caspase-3 positivity.

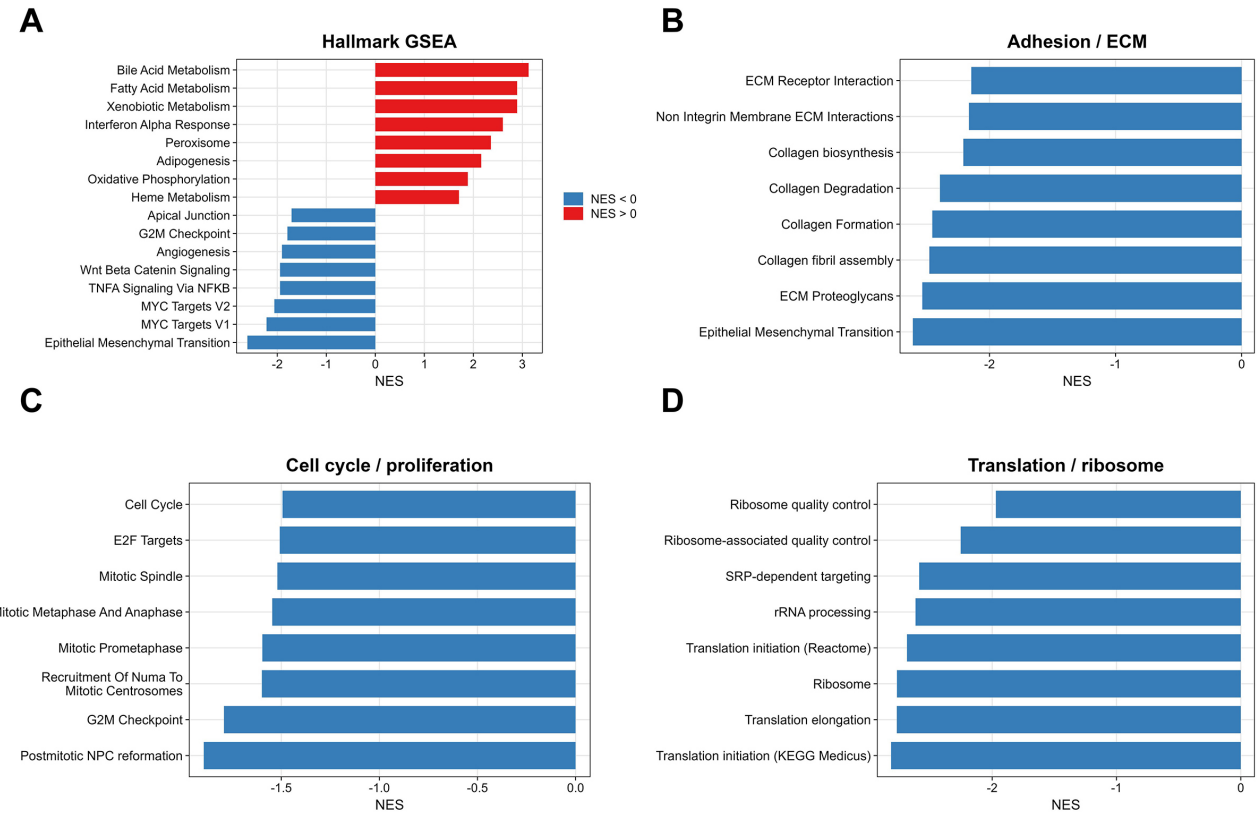

Fig. 5. GSEA-based evaluation of pathway patterns associated with *PDE4DIP* expression in TCGA-LIHC tumors. (A) Overview of selected Hallmark pathways identified through GSEA-based comparisons of median-defined *PDE4DIP*-high and *PDE4DIP*-low tumor samples in the TCGA-LIHC cohort. (B) Selected adhesion- and ECM-related pathways associated with *PDE4DIP* expression. (C) Selected cell-cycle- and proliferation-related pathways associated with *PDE4DIP* expression. (D) Selected translation- and ribosome-related pathways associated with *PDE4DIP* expression. The two translation-initiation entries are derived from Reactome and KEGG Medicus, as labeled. Pathways are ranked according to normalized enrichment score (NES) values. Positive and negative NES values indicate enrichment in the *PDE4DIP*-high and *PDE4DIP*-low groups, respectively.

3.5 PDE4DIP Expression Is Associated With Distinct Transcriptional States in Tumors From the TCGA-LIHC Cohort

To explore whether *PDE4DIP* expression is associated with broader transcriptional programs in HCC tumors, we next conducted a GSEA-based exploration of TCGA-LIHC tumor samples stratified based on *PDE4DIP* expression. Hallmark pathway analysis revealed that several metabolic programs, including bile acid metabolism, fatty acid metabolism, xenobiotic metabolism, peroxisome, oxidative phosphorylation, and heme metabolism, all exhibited positive NES values in the *PDE4DIP*-high group (Fig. 5A). In contrast, the epithelial–mesenchymal transition, apical junction, angiogenesis, G2M checkpoint, MYC targets, WNT/β-catenin signaling, and tumor necrosis factor α (TNFα) signaling via nuclear factor kappa B (NF-κB) programs all exhibited negative NES values, consistent with their enrichment in the *PDE4DIP*-low group (Fig. 5A).

These patterns were reaffirmed through a targeted pathway view. Specifically, adhesion- and ECM-related pathways, including the EMT, ECM proteoglycans, collagen formation, collagen degradation, non-integrin membrane ECM interactions, and ECM receptor interaction pathways, all presented with negative NES values, indicating their enrichment in *PDE4DIP*-low tumors (Fig. 5B). Cell cycle and proliferation-related pathways, including the G2M checkpoint, E2F targets, mitotic spindle, mitotic prometaphase, metaphase/anaphase, and cell cycle pathways, also exhibited negative NES values (Fig. 5C). Negative NES values were similarly observed for translation- and ribosome-related pathways, including the rRNA processing, ribosome, translation initiation, translation elongation, signal recognition particle (SRP)-dependent targeting, and ribosome quality control pathways (Fig. 5D).

No simple linear association was evident between these transcriptional patterns and the MMG8 loss-of-function phenotypes noted above. In the experimental models, MMG8 knockdown reduced proliferation and migra-

tion in Huh7 cells, whereas the MMG8-KO Hepa1-6 clone showed reduced proliferation, tumor growth, and Ki67 positivity, with no significant difference in cleaved caspase-3 positivity between groups (Fig. 2B,C; Fig. 3B; Fig. 4A–D). In bulk TCGA tumors, however, higher total *PDE4DIP* expression was associated with negative NES values for several cell-cycle-, ECM-, and ribosome-related gene sets. Because bulk gene-level *PDE4DIP* expression does not resolve MMG8-specific expression or offer insight into the cellular source of the aggregate signal, these results represent context-dependent transcriptional associations rather than a direct measure of MMG8 activity in human tumors.

4. Discussion

A recent integrative bioinformatics study in HCC highlighted the value of combining GEO-based transcriptomic discovery with cross-database expression validation, survival analysis, and tumor-microenvironment assessment to prioritize candidate genes and potential therapeutic leads [16]. Against this background, the present study distinguishes gene-level *PDE4DIP* expression from the function of one *PDE4DIP*-derived protein product, MMG8. Analyses of public HCC datasets revealed differences in *PDE4DIP* expression between tumor and non-tumor tissues, although the directionality of this difference varied across cohorts. Specifically, the TCGA-LIHC and GSE36376 cohorts exhibited higher *PDE4DIP* expression in tumors, whereas the GSE14520 cohort exhibited the opposite expression pattern. These findings argue against treating total *PDE4DIP* expression as a uniform tumor marker in HCC, instead supporting a more cautious interpretation in which bulk *PDE4DIP* mRNA levels may reflect differences in platform, tissue composition, tumor purity, transcript coverage, or isoform usage. The specific Affymetrix and Illumina probes used in the GSE14520 and GSE36376 analyses could not be confirmed to interrogate identical *PDE4DIP* exons, and neither platform provided MMG8 isoform-specific resolution. In the TCGA-LIHC cohort, gene-level *PDE4DIP* expression was not independently associated with overall survival in the main multivariable model or in fibrosis- and purity-adjusted sensitivity analyses.

To more directly examine the functional role of MMG8 in HCC, a series of complementary functional experiments was conducted. MMG8 knockdown in Huh7 cells reduced proliferation and migration, whereas the MMG8-KO Hepa1-6 clone presented with decreased proliferative capacity prior to subcutaneous inoculation and subsequently formed smaller subcutaneous tumors with lower Ki67 positivity. These findings support a role for MMG8 in maintaining proliferative and migratory behavior in the tested model systems. The concordant *in vitro* and tissue-level proliferation findings suggest that reduced proliferative activity was the more prominent correlate of the *in vivo* phenotype. Cleaved caspase-3 positivity did not differ significantly between control and MMG8-KO tumors, and the endpoint data therefore do not support increased caspase-3-associated apoptosis as an explanation for the reduced tumor growth.

This phenotype is consistent with the known biology of *PDE4DIP*/myomegalin proteins. *PDE4DIP* encodes scaffold proteins linked to Golgi and centrosomal organization, cAMP compartmentalization, and microtubule regulation [17]. MMG8 has been reported to localize to the Golgi and participate in the processes of Golgi microtubule organization and ER-Golgi transport [7]. Such functions provide a plausible framework for the present observations. Cell proliferation and migration require spatial coordination of signaling complexes, cytoskeletal tracks, and membrane trafficking. A scaffold positioned at the Golgi-microtubule interface has the potential to influence these processes without acting as a conventional kinase or transcription factor.

The TCGA GSEA analysis conducted herein added another dimension to this study. *PDE4DIP*-high tumors exhibited positive NES values for several metabolic programs, whereas negative NES values were noted for adhesion/ECM-, cell-cycle/proliferation-, and translation/ribosome-related pathways, indicating enrichment in *PDE4DIP*-low tumors. The association between this pattern and the cell-based loss-of-function phenotype was not a simple linear relationship. If total *PDE4DIP* mRNA perfectly reflected MMG8 activity in tumor cells, *PDE4DIP*-high tumors would be expected to show higher enrichment of growth- or migration-related pathways, which was not the case. The discrepancy likely reflects the difference between bulk tumor transcriptomes and defined experimental models. Recent reviews as well as single-cell and single-nucleus transcriptomic studies have highlighted substantial molecular and microenvironmental heterogeneity in HCC and identified distinct proliferative, metabolic, and EMT-associated malignant cell states [18,19,20,21]. Bulk RNA-seq analyses capture transcriptional signals from malignant cells together with stromal, immune, endothelial, and other non-malignant compartments [22]. Total *PDE4DIP* expression may also fail to capture the abundance, localization, or activity of the MMG8 isoform.

This study has certain limitations. The functional experiments employed a single MMG8-targeting siRNA duplex in Huh7 cells and a single sgRNA-derived MMG8-KO clone together with a single-cell-derived empty-vector control clone in Hepa1-6 cells. Sequence-specific off-target effects and clone-specific effects therefore cannot be fully excluded because additional independent targeting sequences, clones, and genomic target-site sequencing were not used, and rescue experiments were not performed. Because the epitope recognized by the 443M antibody is shared with some larger *PDE4DIP* isoforms, absolute isoform specificity across all tissues cannot be definitively established. No attempt was made to directly examine Golgi morphology, ER-Golgi trafficking, microtubule organiza-

tion, or downstream signaling. Cleaved caspase-3 positivity was assessed at a single endpoint and did not differ significantly between groups; complementary apoptosis assays and additional time points were not evaluated. Survival and metastatic burden were not evaluated in mouse model experiments. GSEA analyses were based on bulk TCGA tumors without any deconvolution of the tumor and non-tumor cellular compartments. Recurrence-free survival could not be assessed because valid recurrence-time data were unavailable, and viral status, etiology, and alcohol history were not available in the clinical annotation used for the present analysis. Fibrosis-related information was available for only a subset of TCGA-LIHC cases, and the fibrosis-adjusted sensitivity analysis was therefore conducted in a reduced sample. Direct MMG8 isoform-specific expression and quantitative protein validation in primary human HCC tissues were also not available. As endpoint tumor weights were not recorded, *in vivo* assessment relied primarily on longitudinal caliper-based tumor-volume measurements, with the corresponding AUC summaries, gross tumor images, and histological analyses serving as supporting readouts. As only female mice were used in these experiments, potential sex-dependent differences in tumor growth and host responses were not assessed, limiting the generalizability of the *in vivo* findings. These limitations define the scope of the conclusion.

5. Conclusions

In summary, gene-level *PDE4DIP* expression is associated with heterogeneous transcriptomic patterns in HCC patient cohorts. MMG8 knockdown reduced proliferation and migration in Huh7 cells, whereas the MMG8-KO Hepa1-6 clone showed reduced proliferation, subcutaneous tumor growth, and Ki67 positivity, with no significant difference in cleaved caspase-3 positivity between groups. These findings support a functional contribution of MMG8 to the phenotypes observed in the selected HCC models while underscoring the distinction between the functional relevance of the MMG8 protein and bulk gene-level *PDE4DIP* expression. Additional isoform-specific validation, rescue experiments, analyses using independent loss-of-function reagents or clones, and mechanistic studies will be required before MMG8 can be considered a general driver or therapeutic target in HCC.

Availability of Data and Materials

The public datasets analyzed in this study are available from TCGA-LIHC and the GEO datasets GSE14520 and GSE36376. Other data supporting the findings of this study are available from the corresponding author upon reasonable request.

Author Contributions

CW: Investigation, Validation, Software, Visualization, Writing - original draft. CB: Methodology, Formal analysis. TL: Conceptualization, Supervision, Project administration, Funding acquisition. All authors contributed to editorial changes in the manuscript. All authors read and approved the final manuscript. All authors have participated sufficiently in the work and agreed to be accountable for all aspects of the work.

Ethics Approval and Consent to Participate

All animal experimental procedures were conducted in accordance with the guidelines of the Animal Ethics Committee of the Laboratory Animal Center, Xuanwu Hospital, Capital Medical University, China, and were approved by the same committee (XW-20210420-10). The principles of the 3Rs (Replacement, Reduction, and Refinement) were followed, and the study was reported in accordance with the ARRIVE guidelines.

Acknowledgment

Not applicable.

Funding

This work was supported by the National Natural Science Foundation of China (Grant No. 82270495).

Conflicts of Interest

The authors declare no conflicts of interest.

Supplementary Material

Supplementary material associated with this article can be found, in the online version, at https://doi.org/10.31083/FBL54109.

References

[1] Villanueva A. Hepatocellular Carcinoma. The New England Journal of Medicine. 2019; 380: 1450–1462. https://doi.org/10.1056/NEJMra1713263

[2] Llovet JM, Kelley RK, Villanueva A, Singal AG, Pikarsky E, Roayaie S, et al. Hepatocellular carcinoma. Nature Reviews. Disease Primers. 2021; 7: 6. https://doi.org/10.1038/s41572-020-00240-3

[3] Cancer Genome Atlas Research Network. Comprehensive and Integrative Genomic Characterization of Hepatocellular Carcinoma. Cell. 2017; 169: 1327–1341.e23. https://doi.org/10.1016/j.cell.2017.05.046

[4] Hoshida Y, Nijman SMB, Kobayashi M, Chan JA, Brunet JP, Chiang DY, et al. Integrative transcriptome analysis reveals common molecular subclasses of human hepatocellular carcinoma. Cancer Research. 2009; 69: 7385–7392. https://doi.org/10.1158/0008-5472.CAN-09-1089

[5] Verde I, Pahlke G, Salanova M, Zhang G, Wang S, Coletti D, et al. Myomegalin is a novel protein of the golgi/centrosome that interacts with a cyclic nucleotide phosphodiesterase. The Journal of Biological Chemistry. 2001; 276: 11189–11198. https://doi.org/10.1074/jbc.M006546200

[6] Roubin R, Acquaviva C, Chevrier V, Sedjaï F, Zyss D, Birnbaum D, et al. Myomegalin is necessary for the formation of centrosomal and Golgi-derived microtubules. Biology Open. 2013; 2: 238–250. https://doi.org/10.1242/bio.20123392

[7] Wang Z, Zhang C, Qi RZ. A newly identified myomegalin isoform functions in Golgi microtubule organization and ER-Golgi transport. Journal of Cell Science. 2014; 127: 4904–4917. https://doi.org/10.1242/jcs.155408

[8] Esseltine JL, Scott JD. AKAP signaling complexes: pointing towards the next generation of therapeutic targets? Trends in Pharmacological Sciences. 2013; 34: 648–655. https://doi.org/10.1016/j.tips.2013.10.005

[9] Reggi E, Diviani D. The role of A-kinase anchoring proteins in cancer development. Cellular Signalling. 2017; 40: 143–155. https://doi.org/10.1016/j.cellsig.2017.09.011

[10] Heath AP, Ferretti V, Agrawal S, An M, Angelakos JC, Arya R, et al. The NCI Genomic Data Commons. Nature Genetics. 2021; 53: 257–262. https://doi.org/10.1038/s41588-021-00791-5

[11] Edgar R, Domrachev M, Lash AE. Gene Expression Omnibus: NCBI gene expression and hybridization array data repository. Nucleic Acids Research. 2002; 30: 207–210. https://doi.org/10.1093/nar/30.1.207

[12] Subramanian A, Tamayo P, Mootha VK, Mukherjee S, Ebert BL, Gillette MA, et al. Gene set enrichment analysis: a knowledge-based approach for interpreting genome-wide expression profiles. Proceedings of the National Academy of Sciences of the United States of America. 2005; 102: 15545–15550. https://doi.org/10.1073/pnas.0506580102

[13] Liberzon A, Birger C, Thorvaldsdóttir H, Ghandi M, Mesirov JP, Tamayo P. The Molecular Signatures Database (MSigDB) hallmark gene set collection. Cell Systems. 2015; 1: 417–425. https://doi.org/10.1016/j.cels.2015.12.004

[14] Carter SL, Cibulskis K, Helman E, McKenna A, Shen H, Zack T, et al. Absolute quantification of somatic DNA alterations in human cancer. Nature Biotechnology. 2012; 30: 413–421. https://doi.org/10.1038/nbt.2203

[15] Hoadley KA, Yau C, Hinoue T, Wolf DM, Lazar AJ, Drill E, et al. Cell-of-Origin Patterns Dominate the Molecular Classification of 10,000 Tumors from 33 Types of Cancer. Cell. 2018; 173: 291–304.e6. https://doi.org/10.1016/j.cell.2018.03.022

[16] Amin A, Fatima S, Aslam MK, Belaidi M, Bibi S, Bufarwa SW, et al. In silico identification of a prognostic gene signature and virtual screening for hepatocellular carcinoma. Computational Biology and Chemistry. 2026; 120: 108718. https://doi.org/10.1016/j.compbiolchem.2025.108718

[17] Mani A. PDE4DIP in health and diseases. Cellular Signalling. 2022; 94: 110322. https://doi.org/10.1016/j.cellsig.2022.110322

[18] Safri F, Nguyen R, Zerehpooshnesfchi S, George J, Qiao L. Heterogeneity of hepatocellular carcinoma: from mechanisms to clinical implications. Cancer Gene Therapy. 2024; 31: 1105–1112. https://doi.org/10.1038/s41417-024-00764-w

[19] Donne R, Lujambio A. The liver cancer immune microenvironment: Therapeutic implications for hepatocellular carcinoma. Hepatology (Baltimore, Md.). 2023; 77: 1773–1796. https://doi.org/10.1002/hep.32740

[20] Alvarez M, Benhammou JN, Darci-Maher N, French SW, Han SB, Sinsheimer JS, et al. Human liver single nucleus and single cell RNA sequencing identify a hepatocellular carcinoma-associated cell-type affecting survival. Genome Medicine. 2022; 14: 50. https://doi.org/10.1186/s13073-022-01055-5

[21] Guo DZ, Zhang X, Zhang SQ, Zhang SY, Zhang XY, Yan JY, et al. Single-cell tumor heterogeneity landscape of hepatocellular carcinoma: unraveling the pro-metastatic subtype and its interaction loop with fibroblasts. Molecular Cancer. 2024; 23: 157. https://doi.org/10.1186/s12943-024-02062-3

[22] Yoshihara K, Shahmoradgoli M, Martínez E, Vegesna R, Kim H, Torres-Garcia W, et al. Inferring tumour purity and stromal and immune cell admixture from expression data. Nature Communications. 2013; 4: 2612. https://doi.org/10.1038/ncomms3612